Nano Energy 59 (2019) 197–206

Contents lists available at ScienceDirect

Nano Energy

journal homepage: www.elsevier.com/locate/nanoen

Full paper

Exceptionally highly stable cycling performance and facile oxygen-redox of manganese-based cathode materials for rechargeable sodium batteries

Aishuak Konarov[a], Jae Hyeon Jo[a], Ji Ung Choi[a], Zhumabay Bakenov[b], Hitoshi Yashiro[c], Jongsoon Kim[a,*], Seung-Taek Myung[a,*]

[a] Department of Nano Technology and Advanced Materials Engineering, Sejong University, Seoul 05006, South Korea
[b] Institute of Batteries LLC, National Laboratory Astana, Nazarbayev University, 53 Kabanbay Ave., Astana 010000, Kazakhstan
[c] Department of Bio-Science and Technology, Iwate University, Morioka 0208550, Japan

ARTICLE INFO

Keywords:
Oxygen-redox
Mn rich
First-principle calculation
Cathode
Sodium ion battery

ABSTRACT

In this study, the effect of Zn doping on the electrochemical properties of P2-$Na_{2/3}[Mn_{1-x}Zn_x]O_2$ (x = 0.0, 0.1, 0.2, 0.3) is investigated for the first time. The P2-$Na_{2/3}[Mn_{0.7}Zn_{0.3}]O_2$ electrode deliveres a specific discharge capacity of approximately 190 mAh g^{-1} based on the oxygen-redox reaction (O^{2-}/O^{1-}), after which the Mn^{4+}/Mn^{3+} redox reaction contributes to the capacity. The cycling performance of the P2-$Na_{2/3}[Mn_{0.7}Zn_{0.3}]O_2$ electrode is also greatly enhanced compared with that of the P2-$Na_{2/3}MnO_2$ electrode (capacity retention of 80% vs. 30% after 200 cycles). This improved cyclability is due to the suppression of cooperative Jahn–Teller distortion as well as stabilization of the structure by the electrochemically inactive Zn^{2+} ions. First-principle calculations and experimental analysis, including X-ray photoelectron spectroscopy and X-ray absorption near edge structure spectroscopy, clearly confirms that the Zn^{2+} substitution in P2-$Na_{2/3}MnO_2$ enables the O^{2-}/O^{1-} redox reaction. In addition, time-of-flight secondary ion mass spectroscopy analysis reveals that no sodium carbonates forms on the electrode surface. Our findings provide a potential new path to utilize cost-effective Mn-rich cathode materials for sodium-ion batteries via not only cationic redox but also anodic redox.

1. Introduction

The recent construction of Gigafactories in the US and Germany reflects the significant increasing demand for lithium-ion batteries (LIBs) [1–3]. In addition, as the Paris Agreement aims to mitigate climate change by moving toward the generation of electricity from non-fossil fuels in the upcoming ten years [4], there is an urgent need for more green power sources. Although LIBs are the most suitable power sources for both portable and stationary applications, the main recent issue is that lithium resources are unevenly distributed and can be politically controlled, thereby affecting their price. One of the best alternative candidates for LIBs is sodium-ion batteries (SIBs), especially for energy storage applications. Sodium is the sixth most abundant element on the earth's crust, making sodium resources more cost effective than lithium resources. Although the chemical potential of Na is slightly higher than that of Li (approximately 0.3 V vs. the standard hydrogen electrode), their similar chemistries and adoption of intercalation, conversion, and alloy reactions make SIBs very attractive alternatives to LIBs [5,6].

Two-dimensional layered sodium transition metal oxides have been widely studied because of their high capacities [7]. They are represented as O3- and P2-type structures, where O and P denote the location of the sodium ion in the structure (P: prismatic site, O: octahedral site) and the numbers indicate the number of transition metal layers in a unit cell of the structure [8]. P2-type compounds generally deliver higher discharge capacity than O3-type materials [9]. Among P2-type materials, manganese-based ($Na_{2/3}MnO_2$) cathode materials are particularly attractive because of the low cost of manganese resources and the high discharge capacity (> 200 mAh g^{-1}) of these materials compared with other P2-type materials [10]. However, manganese-based cathode materials exhibit poor long-term cyclability because of the presence of Mn^{3+} ions, Jahn–Teller ions that cause elongation of the Mn–O bond length along one specific direction. This asymmetry in the crystal structure results in structural disintegration, leading to rapid capacity fading during cycling. This anisotropic change in the structure can be overcome by dilution of the Mn^{3+} concentration by substituting Mn^{3+} with other electroactive or inactive species [11–16].

Electro-inactive magnesium has been used to suppress the Jahn–Teller distortion caused by Mn^{3+} ions in the crystal structure

* Corresponding authors.
E-mail addresses: jongsoonkim@sejong.ac.kr (J. Kim), smyung@sejong.ac.kr (S.-T. Myung).

https://doi.org/10.1016/j.nanoen.2019.02.042
Received 24 November 2018; Received in revised form 16 February 2019; Accepted 17 February 2019
Available online 19 February 2019

[17–20]. Cléments and coworkers reported partial substitution of Mn^{3+} ions by Mg^{2+} to stabilize the crystal structure [17]. Improved electrochemical performance with a smooth voltage profile was achieved with only 5% substitution of Mg^{2+} at the Mn^{3+} site. The authors suggested that the Mg doping was responsible for suppression of the Jahn–Teller distortion and enhanced the structural stability with cycling [17]. In earlier work, Yabuuchi and coworkers [18] introduced a high concentration of Mg^{2+} (up to 28%) in P2-$Na_{2/3}MnO_2$, substituting almost all of the Mn^{3+} ions, leading to the formation of $Na_{2/3}[Mn_{0.72}Mg_{0.28}]O_2$, with an Mn oxidation state close to 4 + [18]. Unexpectedly, the inactive material, $Na_{2/3}[Mn^{3.84+}_{0.72}Mg^{2+}_{0.28}]O_2$, delivered a charge capacity of approximately 150 mAh g^{-1} and a discharge capacity of over 200 mAh g^{-1} in the following cycles. Considering the $Mn^{3+/4+}$ redox on charge, delivery of such a large capacity cannot be explained by the $Mn^{3+/4+}$ redox. This anomalous large reversible capacity was thought to originate from the oxygen redox during the first charge. The Mn^{4+} is then reduced to Mn^{3+} on discharge in the following cycles and vice versa, similar to in the Li_2MnO_3 system [18]. The large hysteresis between the charge and discharge curves indicates the possibility of oxygen redox during the first charge, as oxygen redox exhibit high polarization. Recently, Maitra and coworkers confirmed that $Na_{2/3}[Mn_{0.72}Mg_{0.28}]O_2$ undergoes an oxygen redox reaction [21]. Indeed, the oxygen redox $O^{2-/1-}$ activated by the oxygen of transition metals does not require the presence of alkali ions in the transition metal layer.

Divalent Zn has recently been used as a dopant to stabilize the structure of P2-$Na_{2/3}MnO_2$. Wu et al. [22] studied the effect of Zn doping on P2-type $Na_{0.66}Ni_{0.33-x}Zn_xMn_{0.67}O_2$ (x = 0, 0.07, 0.14). The overall electrochemical properties of the Zn-doped material improved even though Zn remained as the electro-inactive species during the electrochemical reaction. The inactive divalent Zn likely suppressed the Na^+/vacancy ordering, producing a smooth voltage profile. Later, these researchers observed that an additional structural transformation, mainly a transition from the P2 to P′2 structure, occurred for Zn-free P2-type $Na_{0.66}Ni_{0.33}Mn_{0.67}O_2$, whereas such behavior was suppressed in Zn-doped $Na_{0.66}Ni_{0.26}Zn_{0.07}Mn_{0.67}O_2$ [23]. As a result, the Zn-doped electrode exhibited better electrode performances over cycles. Aguesse et al. [24] reported the effect of Zn^{2+} ion substitution on layered $Na_3Ni_2SbO_6$. Ni^{2+} ions were partially substituted by Zn^{2+} ions in the structure, and the Zn-substituted material ($Na_3Ni_{1.5}Zn_{0.5}SbO_6$) exhibited improved electrochemical performance, maintaining 80% of its initial capacity after 50 cycles, compared with that of the undoped material. Moreover, the Zn doping affected the phase transition at high voltage, which led to a smooth voltage profile. Xu et al. [25] showed that Zn doping can stabilize the structure by comparing P2-type $Na_{0.67}Mn_{0.6}Fe_{0.4}O_2$ and $Na_{0.67}Mn_{0.6}Fe_{0.3}Zn_{0.1}O_2$. Zn doping minimized the polarization and improved the electrochemical properties of $Na_{0.67}Mn_{0.6}Fe_{0.4}O_2$. In addition, Zn doping suppressed the Jahn–Teller distortion owing to the dilution of the Mn^{3+} concentration in the structure by Zn^{2+} ions. Kumakura et al. [26] demonstrated the effect of metal substitution on the electrochemical properties of P′2-$Na_{2/3}Mn_{0.9}Me_{0.1}O_2$ (Me = Mg, Ti, Co, Ni, Cu, and Zn) compounds. Differentiated plots revealed that doping with Zn resulted in a smoother voltage profile than doping with the other metals.

The above literature review demonstrates the effectiveness of doping with divalent Zn in stabilizing the crystal structure, which is promising for retention of the initial capacity during cycling. Motivated by this review, we, for the first time, studied the effect of Zn doping on P2-type $Na_{2/3}[Mn_{1-x}Zn_x]O_2$ over the wide range of $0 \le x \le 0.3$ to better understand the role of Zn^{2+} on the structure and electrochemical properties of this system. Because the oxidation state of manganese in the 30% doped material ($Na_{2/3}[Mn_{0.7}Zn_{0.3}]O_2$) is close 4 +, it should be electrochemically inactive as the Mn^{4+}/Mn^{5+} redox is not possible within the normal operation window (1.5 – 5 V vs. Na^+/Na). However, this material delivered a capacity of approximately 120 mAh g^{-1} at the first charge. First-principles calculations indicated that Zn substitution at Mn sites in P2-$Na_{2/3}MnO_2$ led to the O^{2-}/O^{1-} redox reaction. In addition to the observation of Mn^{4+} ions in the structure, changes in the local atomic environments and electronic states of O ions arose when a particular Zn–O–Na configuration replaced the general Mn–O–Na configuration in P2-$Na_{2/3}MnO_2$. X-ray adsorption spectroscopy analysis confirmed that the O^{2-}/O^{1-} redox is reversible, after which Mn^{4+}/Mn^{3+} contributes to the electrochemical activity. More interestingly, the cycling performance of the P2-type $Na_{2/3}MnO_2$ electrode was improved with the presence of Zn^{2+} in the crystal structure. We herein discuss the effect of Zn^{2+} doping in $Na_{2/3}[Mn_{1-x}Zn_x]O_2$, $0 \le x \le 0.3$ on the crystal structure, electrochemistry, and electrochemical mechanism.

2. Experimental

2.1. Synthesis of materials

The P2-$Na_{2/3}[Mn_{1-x}Zn_x]O_2$ (x = 0, 0.1, 0.2, 0.3) samples were prepared using a combustion method described in our previous work [27]. Hereafter, the $Na_{2/3}[Mn_{1-x}Zn_x]O_2$ samples are denoted as Z0, Z1, Z2, and Z3 for x = 0, 0.1, 0.2, and 0.3, respectively. First, appropriate amounts of sodium nitrate (98%, Aldrich), manganese(II) nitrate hexahydrate (97%, Aldrich), and zinc(II) nitrate hexahydrate (98%, Aldrich) were dissolved in distilled water and continuously added to an aqueous citric acid solution with a ratio of 1:0.5 by weight (nitrates:citric acid). The solution was heated on a hot plate at 100 °C overnight under constant stirring to evaporate the used solvents. Then, the dried powders were further heated to 200 °C for the auto-combustion of citric acid. The powders were then heated at 500 °C for 3 h to decompose the organic compounds, and the obtained powders were pelletized and heated in a tube furnace at 700 °C (except Z0, which was heated at 900 °C) for 10 h in air and then slowly cooled to room temperature. The obtained powder was transferred to an Ar-filled glove box to avoid contact with moisture in the air.

2.2. Characterization

X-ray diffraction (XRD; X′Pert, PANalytical) using Cu-Kα radiation was employed to characterize the crystal structure of the synthesized powders. The XRD measurements were performed in the 2θ range of 10 − 110° with a step size of 0.03°. The FullProf Rietveld program [28] was used to analyze the powder diffraction patterns. X-ray photoelectron spectroscopy (XPS; PHI 5600, Perkin-Elmer, USA) measurements were performed in macro mode (3 × 3 mm^2) using an Mg X-ray source. The samples (pristine, charged, after 1 cycle) were first transferred to a hermitically sealed transfer chamber (ULVAC) in a glove box and then transferred to the vacuum chamber of the XPS machine to prevent exposure to air or water molecules during the XPS measurement. The XPS spectra were fitted using a non-linear least squares fit with a Gaussian peak shape, and the Shirley method was used to subtract the background before each fit. The binding energies of the Mn 2p, O 1s, and C 1s levels of the electrodes were calibrated with respect to the C 1s peak at 284.6 eV. To identify the surface states, we analyzed the P2-$Na_{2/3}[Mn_{0.7}Zn_{0.3}]O_2$ electrode using time-of-flight secondary ion mass spectroscopy (ToF-SIMS; nanoTOF), equipped with a liquid Ga^+ ion source and pulse electron flooding operated at 10^{-9} Torr. During the analysis, the targets were bombarded by 10-keV Ga^+ beams with a pulsed primary ion current varying from 0.3 to 0.5 pA.

The *ex situ* XAS measurements for Mn K edge spectra were performed at the 7D beamline at the Pohang Accelerator Laboratory (PAL), Pohang, South Korea, and have the five energy steps with different integration time; first energy step and integration time: 5 eV and 1 s, second energy step and integration time: 2.5 eV and 1 s, third energy step and integration time: 0.2 eV and 1 s, fourth energy step and integration time: 0.03 keV and 1 s, and fifth energy step and integration time: 0.04 keV and 1 s from 6339.002 eV (E_0). The spectra for the O K-edge were measured using a synchrotron radiation photoemission

spectroscopy with the incident X-ray source at 650 eV and have three energy steps with different integration time; first energy step and integration time: 0.3 eV and 1 s, second energy step and integration time: 0.2 eV and 1 s, and third energy step and integration time: 0.4 keV and 1 s from 525.000 eV (E_0) at the 4D beam line at the Pohang Accelerator Laboratory (PAL), Pohang, South Korea. The raw XAS data were corrected for pre-edge and post edge background and normalized to unit step height. The X-ray absorption near-edge structure (XANES) data were analyzed using the Athena software package [29].

2.3. Electrochemical tests

To fabricate the positive electrode, the prepared active materials were mixed with conducting materials Super-P and polyvinylidene fluoride in *N*-methyl-2-pyrrolidone (NMP) in a weight ratio of 8:1:1. The obtained slurry (typically 3.0 mg cm^{-2}) was applied on Al foil and dried at 80 °C overnight under vacuum before use. Electrochemical cell tests were conducted after assembling a R2032 coin-type cell using sodium metal as the negative electrode in an Ar-filled glove box. The electrolyte solution consisted of 0.5 M $NaPF_6$ in propylene carbonate and fluorinated ethylene carbonate (PC:FEC, 98:2 by volume). The cells were charged and discharged between 1.5 and 4.6 V at a current density of 26 mA g^{-1} at 25 °C. The galvanostatic intermittent titration technique (GITT) was employed at a pulse of 26 mA g^{-1} for 1 h and with 2 h relaxation time between each pulse.

2.4. Computational details

All the calculations were performed using density functional theory (DFT) calculations and the projector augmented-wave (PAW) method implemented in the Vienna ab initio simulation package (VASP) [30–32] and employed a plane wave basis set with energy cutoff of 500 eV. We used PAW pseudopotentials [33] with a plane-wave basis set as implemented in VASP. Perdew–Burke–Ernzerhof (PBE) parameterization of the generalized gradient approximation (GGA) [34] was used for the exchange-correlation functional. The U value of Mn for the GGA + *U* based DFT calculation was 3.9 eV [35]. The lattice parameters and atomic positions of all the structures were optimized until the residual forces were smaller than 0.05 eV Å − 1. To investigate the oxygen redox activity of Zn-substituted P2-$Na_{0.67}MnO_2$, we used the simplified crystal structure of P2-$Na_{0.5}Mn_{0.75}Zn_{0.25}O_2$ with a 2 × 2 × 1 supercell. The Zn/Mn ordering and Na/vacancy ordering for preparation of the P2-$Na_{0.5-x}Mn_{0.75}Zn_{0.25}O_2$ structure were determined by comparison of the electrostatic energies and DFT energies for 20 Zn/Mn ordering or Na/vacancy ordering arrangements using CASM software [36]. For calculation of the density of states (DOS), the Heyd–Scuseria–Ernzerhof hybrid functional (HSE06) was used, as it has been observed to reproduce the O 2*p* states for transition metal oxides.

3. Results and discussion

The calculated XRD patterns of the samples were obtained by Rietveld refinement using the FullProf software, as shown in Fig. 1a. All the samples were well matched with the P2-type structure (Fig. 1b) with $P6_3/mmc$ space group, with an acceptable reliability factor (R_{wp}) of approximately 10%. An increase in the concentration of Zn^{2+} ions in the crystal structure led to a linear increase in the lattice parameters, as observed in Fig. 1c, obeying Vegard's law. As Zn^{2+} (74 pm) ions have a larger Shannon ionic radius than Mn^{3+} ions (64.5 pm) and Mn^{4+} ions (53 pm), the linear increases in the parameters are reasonable for Zn-doped $Na_{2/3}[Mn_{1-x}Zn_x]O_2$ (x = 0, 0.1, 0.2, 0.3). In addition, the Zn ions can be situated at the Mn^{3+} sites rather than the Mn^{4+} sites because of the preference of ionic size. The XANES data confirm the assumption that the average oxidation state of manganese increased with Zn doping (Fig. 1d) with minor variations in Mn pre-edge (inset of Fig. 1d). The chemical compositions of the materials were confirmed using ICP, as shown in Table S1.

Fig. 2 shows the electrochemical performance of the P2-$Na_{2/3}[Mn_{1-x}Zn_x]O_2$ (x = 0.0, 0.1, 0.2, 0.3) electrodes tested at a constant current of 26 mA g^{-1} in the range of 1.5–4.6 V. From the voltage profiles for the initial cycle (Fig. 2a), it can be observed that the Zn-free electrode, Z0, delivered a capacity of approximately 90 mAh $(g\text{-oxide})^{-1}$ on charge (oxidation) and 180 mAh g^{-1} on discharge (reduction). Unfortunately, the capacity retention was poor, which is most likely associated with the Jahn–Teller distortion in the oxide matrix. Notably, the charge profiles of the Zn-doped $Na_{2/3}[Mn_{1-x}Zn_x]O_2$ electrodes differed from that of the Zn-free electrode for the initial cycle. As indicated by the XANES data (Fig. 1d), Zn substitution resulted in an increase in the oxidation state of Mn, which contributed to the $Mn^{3+/4+}$ redox reaction over the entire operation range. This finding indicates that the charge capacity should be reduced with increasing Zn concentration in $Na_{2/3}[Mn_{1-x}Zn_x]O_2$. Such a tendency is observed until 4 V, above which a long plateau that is elongated with increasing Zn content is observed for the Z1, Z2, and Z3 electrodes. In particular, the Z3 electrode exhibited a negligible capacity below 4 V but a capacity of 115 mAh g^{-1} above 4 V. The resulting discharge capacity was approximately 190 mAh g^{-1}. Again, the average oxidation state of Mn for the Z3 electrode was 3.9+, such that the deliverable capacity is theoretically expected to be 26 mAh g^{-1} in the voltage range. ICP results of charged Z3 electrode indicated extraction of Na^+ (~0.42 mol) from the crystal structure (Table S2). In addition, dQ/dV plots for the initial two cycles confirm unusual reversible oxidation above 4 V for the Z1, Z2, and Z3 electrodes (Fig. S1) and reduction during discharge at 3.1 V, 3.0 V and 2.75 V, respectively, which suggests possibility of oxygen redox. In addition, the smoothening of the voltage profiles (Fig. 2a and Fig. S2) and dQ/dV curves suggests suppression of the phase transition and Jahn–Teller distortion effect with increasing Zn concentration in $Na_{2/3}[Mn_{1-x}Zn_x]O_2$, which originates from the reduced Mn^{3+} concentration in the crystal structure. The Zn substitution also affects the cycling performance (Fig. 2b). Among the tested samples, the Z3 electrode exhibited the best cyclability with a capacity retention of 80% after 200 cycles, whereas the Z0 electrode only retained 30% of the initial capacity after 200 cycles. In addition, Z3 electrode illustrated better rate performance than Z0 electrode (Fig. 2c and d). The cyclability most likely improved because of the existence of electrochemically inert Zn^{2+} in the crystal structure, which mitigates the Jahn–Teller distortion by sharing the oxygen connected with Mn^{3+}, O–Zn^{2+}–O–Mn^{3+}–O, thereby preventing anisotropic elongation of the Mn–O bond.

To predict the effect of Zn substitution on the oxygen-redox (O^{2-}/O^{1-}) reaction in the P2-$Na_{2/3}MnO_2$ structure, the projected density of states (pDOS) for the O 2*p* and Mn 3*d* states of the three P2-$Na_{0.5}Mn_{1-x}Zn_xO_2$ samples (x = 0, 0.125, 0.25) were calculated using the Heyd–Scuseria–Ernzerhof (HSE06) hybrid functional, which provides an accurate description of the electronic structures. As observed in Fig. 3a–c, whereas the pDOS on P2-$Na_{0.5}MnO_2$ and P2-$Na_{0.5}Mn_{0.875}Zn_{0.125}O_2$ below the Fermi level (E_F) was significantly affected by the 3*d* orbitals of the Mn ions, the pDOS of the O 2p state dominantly contributed to the electronic structure of P2-$Na_{0.5}Mn_{0.75}Zn_{0.25}O_2$ below the E_F with negligible 3*d* orbitals of Mn ions. This finding implies that the O^{2-}/O^{1-} reaction occurs in P2-$Na_{0.5}Mn_{0.75}Zn_{0.25}O_2$ because of the existence of the Zn–O–Na configuration in the structure. Fig. 3d presents a visualization of the charge density around the O ion in the energy range between 0 and −1 eV, verifying the large charge density corresponding to the isolated O 2p orbital along the direction of linear Zn–O–Na bonding. We supposed that because the Zn ion cannot provide the electron during the redox-reaction (similar to Li or Na ions), an increase in Zn–O–Na bonding may also result in unstable oxygen electrons for the O^{2-}/O^{1-} reaction with minimized effect of Mn ions, similar to the oxygen-redox reaction arising from the Li–O–Li configuration in Li-excess layered structures such as Li_2MnO_3 [35]. Furthermore, Fig. 4 shows that compared with

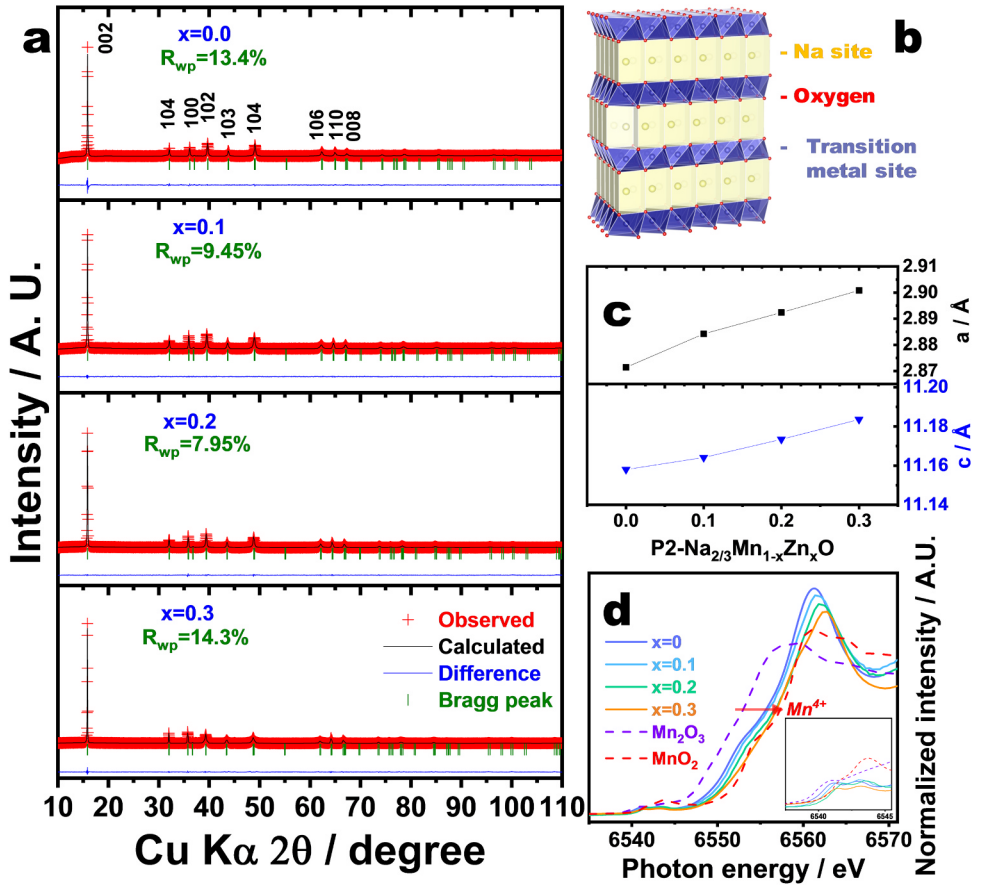

Fig. 1. (a) Rietveld refinement of crystal structure, (b) crystal structure, (c) lattice parameters, and (d) XANES spectra of P2-$Na_{2/3}[Mn_{1-x}Zn_x]O_2$ (x = 0.0, 0.1, 0.2, and 0.3) samples.

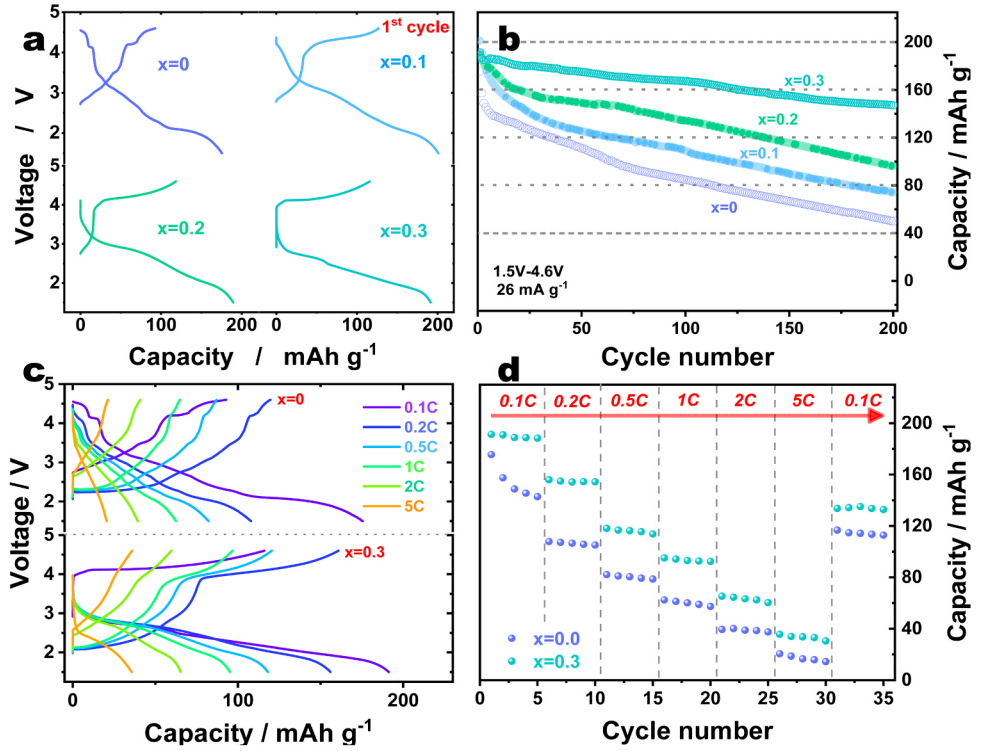

Fig. 2. Electrochemical properties of P2-$Na_{2/3}[Mn_{1-x}Zn_x]O_2$ (x = 0–0.3); (a) first charge –discharge profiles, (b) cycleability, (c) charge and discharge curves at different currents, and (d) short term cyclability at different currents for P2-$Na_{2/3}MnO_2$ and P2-$Na_{2/3}[Mn_{0.7}Zn_{0.3}]O_2$.

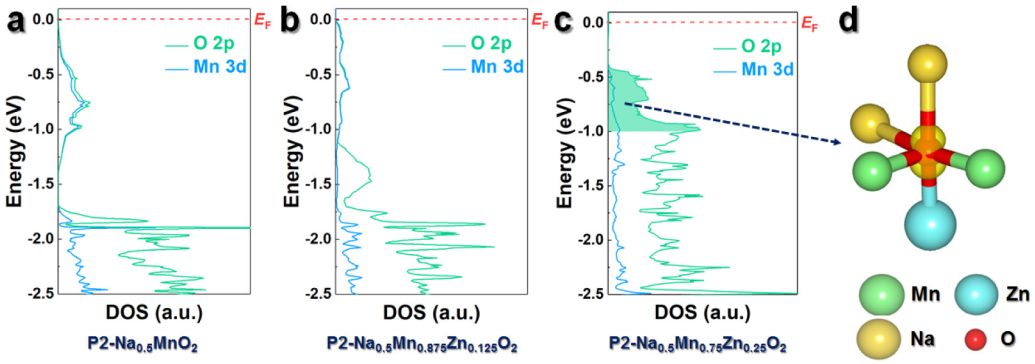

Fig. 3. pDOS of O 2p and Mn 3d orbitals for (a) P2-$Na_{0.5}MnO_2$, (b) P2-$Na_{0.5}Mn_{0.875}Zn_{0.125}O_2$, and (c) P2-$Na_{0.5}Mn_{0.75}Zn_{0.25}O_2$ and (d) spatial electron density (yellow) of P2-$Na_{0.5}Mn_{0.75}Zn_{0.25}O_2$ for -1.0 eV $< E <$ 0 eV. (For interpretation of the references to color in this figure legend, the reader is referred to the web version of this article.)

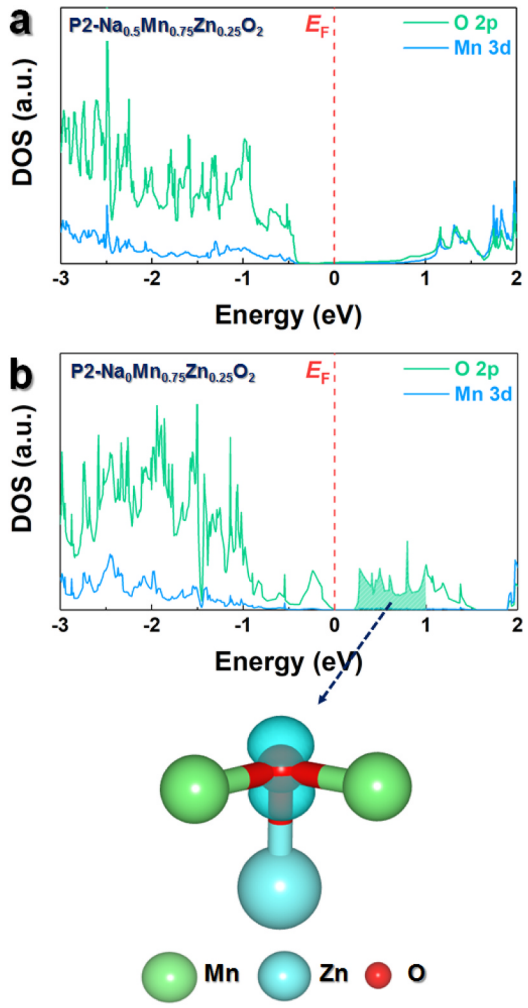

Fig. 4. pDOS of O 2p and Mn 3d orbitals for (a) P2-$Na_{0.5}Mn_{0.75}Zn_{0.25}O_2$ and (b) fully desodiated P2-$Na_0Mn_{0.75}Zn_{0.25}O_2$ and spatial hole density (yellow) of P2-$Na_0Mn_{0.75}Zn_{0.25}O_2$ for 0 eV $< E <$ 1 eV. (For interpretation of the references to color in this figure legend, the reader is referred to the web version of this article.)

P2-$Na_{0.5}Mn_{0.75}Zn_{0.25}O_2$ (Fig. 4a), the desodiated P2-$Na_0Mn_{0.75}Zn_{0.25}O_2$ has an unoccupied state of O 2p orbitals above E_F and the pDOS of the Mn 3d orbital near E_F is negligible (Fig. 4b and c), indicating that Na deintercalation from P2-$Na_{0.5}Mn_{0.75}Zn_{0.25}O_2$ to P2-$Na_0Mn_{0.75}Zn_{0.25}O_2$ is dominant for the O^{2-}/O^{1-} reaction.

Operando XRD (O-XRD) analysis of the Z0 and Z3 electrodes was performed to obtain information on the structural change during the initial charge/discharge and charge process, as depicted in Fig. 5. For the Z0 electrode, during charge, the P2 (002) and P2 (004) peaks

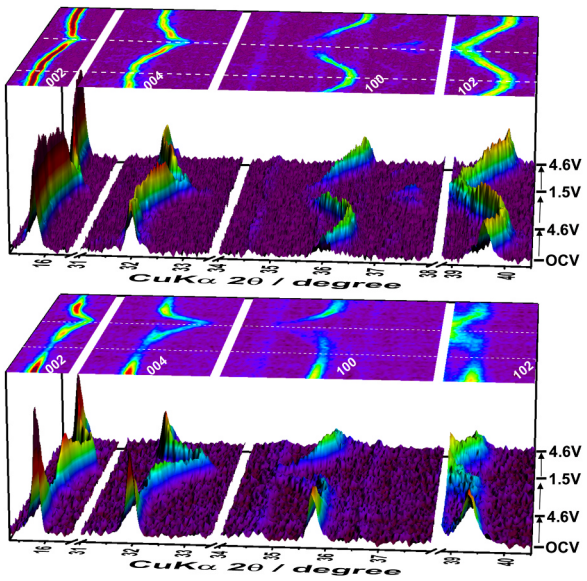

Fig. 5. *Operando* XRD patterns of (a) P2-$Na_{2/3}MnO_2$ and (b) P2-$Na_{2/3}[Mn_{0.7}Zn_{0.3}]O_2$ electrodes.

shifted toward lower angle, whereas the P2 (100) and (102) peaks gradually shifted toward higher angles (Fig. 5a and Fig. S3). This behavior matches well with the calculated lattice parameters, as the c-axis increased and the a-axis decreased with the extraction of Na^+ ions from the crystal structure (Fig. S4a). The resulting composition can be written as $Na_{0.33}MnO_2$ after charging to 4.6 V. During discharge, the reversible process occurred at 2.2 V. However, the P2 peak intensities decreased, and a new phase appeared at 37.5° 2θ below 2.2 V, which is associated with the formation of a new P′2 phase when the sodium content in the structure is higher than 0.7 in Na_xMnO_2, reaching $Na_{1.0}MnO_2$ [37]. In this structure, the Jahn–Teller Mn^{3+} ions are dominant in the transition metal layer after discharging to 1.5 V. The same tendency as the first charge was observed during the second charge.

Unlike for the Z0 electrode, the relative intensities of the P2 phase peaks for the Z3 electrode decreased abruptly above 4.2 V, which is associated with the formation of another phase (Fig. 5b, Figs. S3 and S4b). *Ex situ* XRD measurements of the charged electrode revealed that the formed phase was an OP4 phase, $Na_{0.24}[Mn_{0.7}Zn_{0.3}]O_2$, after charge to 4.6 V (Fig. S5). Because of the very low intensity of the OP4 phase, it was not possible to detect the OP4 phase during the O-XRD measurement. However, it is not possible that the average oxidation state of Mn was 4.51+ after charging to 4.6 V because the oxidation state of Mn cannot exceed 4+ in this operation range. This issue will be discussed in detail in the XPS analysis section. During discharge, the OP4 phase transformed to the original P2 phase (2.2 V), and the resulting intensities increased. Upon further discharging, the P2 peaks

progressively shifted toward higher angle, and the phase was split into two phases: the P2 phase, though not evident at the end of discharge, and the P′2 phase with relatively low intensity compared with that for Z0. At the end of discharge, the composition was approximately $Na_{0.97}[Mn_{0.7}Zn_{0.3}]O_2$ (average oxidation state of Mn: 3.5+), for which the amount of sodium was lower but the oxidation state of Mn was higher than those of Z0, $Na_{1.0}Mn^{3+}O_2$. Note the difference in the oxidation states of Mn for both fully discharged $Na_{1.0}Mn^{3+}O_2$ and $Na_{0.97}[Mn_{0.7}Zn_{0.3}]O_2$. The high oxidation state of Mn is likely to have less affect on the elongation of the Mn–O bond in the crystal structure because of the low concentration of Jahn–Teller Mn^{3+} ions. As observed in Fig. 2a, the delivered capacity for the second charge was approximately 190 mAh g^{-1} for $Na_{0.24}[Mn_{0.7}Zn_{0.3}]O_2$, for which the average oxidation state of Mn is theoretically 4.51+. Again, we cannot explain the variation of the oxidation for Mn above 4+ on charge; specifically, the oxidation state of Mn is given as 4.51+ at the second charge, which is not valid considering the oxidation limit of Mn^{4+} based on the $Mn^{3+/4+}$ redox pair. The P′2 phase was gradually transformed into the P2 phase and finally to the OP4 phase at higher voltage (4.6 V) during the second charge, demonstrating the reversible phase transition: P′2 ↔ P2 ↔ OP4. The high oxidation of Mn on discharge is advantageous to avoid deterioration of the crystal structure resulting from anisotropic variation of the Mn–O bond by Mn^{3+} during prolonged cycling. It is apparent from the *ex situ* XRD analysis after the 1st, 5th, and 10th cycles (Fig. S6 and Table S3) that the P2-type layered structure remained stable over cycles. In addition, the ICP and TOF-SIMS results (Table S2 and Fig. S8) confirm that both zinc and manganese ions remained in the structure.

The Z0 and Z3 electrodes were further analyzed using XPS and XANES to understand the surface and chemical states (Fig. 6 and Fig. S7). Fig. S7a shows the carbon 1s, oxygen 1s, and manganese 2p regions for the Z0 electrode. In the OCV state, the C1s spectra contained the usual peaks corresponding to the C–C bond at 284.6 eV from the conductive agent and C=O and C–O bonds from surface deposited species [38]. For the O1s spectra, a sharp peak is observed at 529.5 eV, which is associated with O^{2-} from the crystal structure of $Na_{2/3}MnO_2$. The two other peaks are related to the surface deposited moieties related to oxygen. The C1s and O1s spectra did not change during charge/discharge, indicating that they do not participate in the electrochemical reaction. Based on the results of chemical composition obtained from ICP and XANES in which the K edge spectrum of Mn for the $Na_{2/3}MnO_2$ locates more close to Mn_2O_3, we assume that the average oxidation state of Mn is close to 3.33+ for the fresh $Na_{0.67}MnO_2$ (Table S1). As anticipated, the oxidation state of Mn shifted to higher energy when charging to 4.6 V (Fig. 6a). Upon discharging to 1.5 V, the corresponding Mn spectrum overlaid that of the Mn_2O_3 reference; however, the state was lower than that of the fresh electrode, indicating that the oxidation state of Mn was close to Mn^{3+}. This finding agrees with the *O*-XRD data presented in Fig. 5a, which shows that $Na_{1.0}MnO_2$ has the oxidation state of Mn^{3+} and that the full sodiation stabilizes the P′2 structure. These variations in the Mn K-edge reveal that the related reaction is the $Mn^{3+/4+}$ redox reaction accompanied by Na^+ de-/intercalation.

For the Z3 electrode, the Mn K-edge spectra reveal that the average oxidation state of Mn is close to 4+ in the fresh state (Fig. 6b). Surprisingly, there was no evident change in the oxidation state of Mn during charge, although a capacity of 120 mAh g^{-1} was delivered. Compared with the fresh electrode, there was almost no difference in the oxidation state of Mn for the charged electrode, except for the slight variation in the pre-edge (inset of Fig. 6b). Similar tendency was observed in $Li[Ni_{0.17}Li_{0.2}Co_{0.07}Mn_{0.56}]O2$ (~300 mAh g^{-1} on charge in which oxygen redox contributed to ~ 200 mAh g^{-1}) reported by Ito et al. [39], although the evolution of the pre-edge was less noticible than that of $Li[Ni_{0.17}Li_{0.2}Co_{0.07}Mn_{0.56}]O_2$ because of the small charge

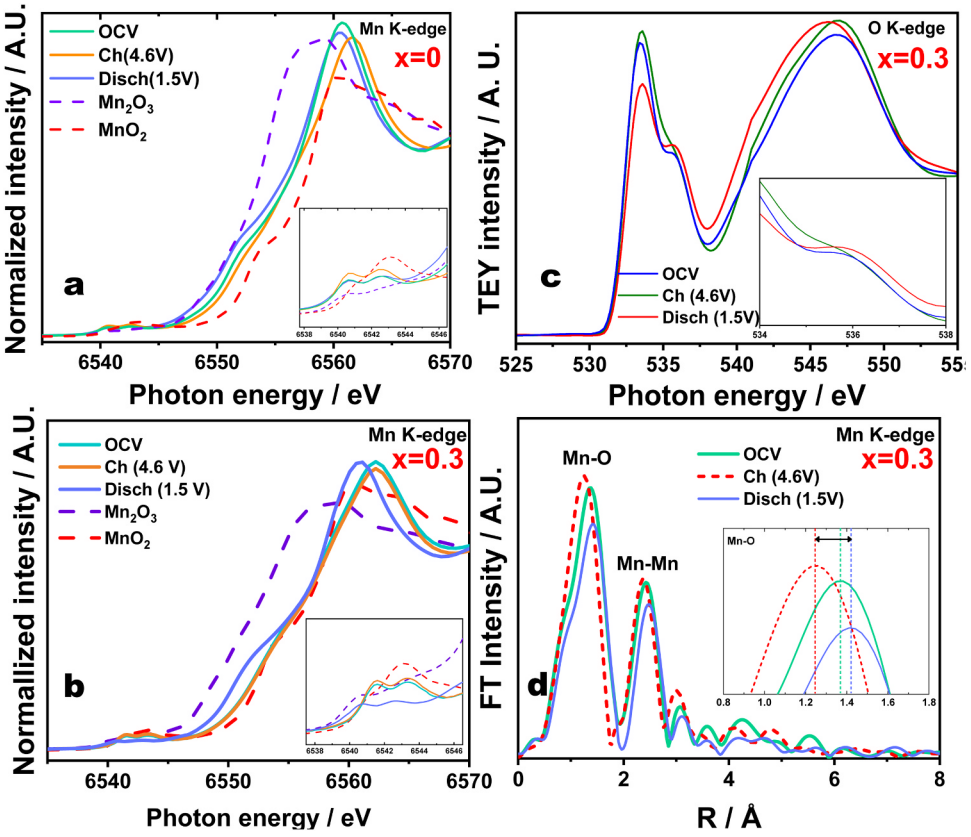

Fig. 6. *Ex situ* XANES spectra before and after first charge and discharge; (a) Mn K edge for P2-$Na_{2/3}MnO_2$; (b) Mn K edge and (c) O K edge of P2-$Na_{2/3}[Mn_{0.7}Zn_{0.3}]O_2$; (d) EXAFS data of Mn for P2-$Na_{2/3}[Mn_{0.7}Zn_{0.3}]O_2$ before and after first charge and discharge.

capacity 120 mAh g^{-1} for the present $Na_{2/3}[Mn_{0.7}Zn_{0.3}]O_2$. The charged electrode can be expressed as $Na_{0.24}[Mn_{0.7}Zn_{0.3}]O_2$, for which the average oxidation state of Mn is theoretically 4.51 +. Note that the Mn cannot be oxidized above the oxidation state of 4+ in the range of 1.5–4.6 V vs. Na^+/Na. After discharging to 1.5 V, the Mn spectrum shifted to lower photon energy, although the energy was still higher than that of Mn_2O_3 and the sodiated $Na_{1.0}MnO_2$. This finding validates the high oxidation state of $Na_{0.97}[Mn_{0.7}Zn_{0.3}]O_2$ (average oxidation state of Mn: 3.5 +) even after discharge to 1.5 V, whereas that of the Mn for $Na_{1.0}MnO_2$ was 3 + . The discrepancy in the oxidation state of Mn at the first charge arises because the charge capacity should have been less than 26 mAh g^{-1} based on the oxidation state of Mn, 3.9+, for $Na_{2/3}[Mn_{0.7}Zn_{0.3}]O_2$ with consideration of the $Mn^{3+/4+}$ redox. In addition, the obtained capacity was approximately 120 mAh g^{-1}, giving $Na_{0.24}[Mn^{4.51+}_{0.7}Zn_{0.3}]O_2$ after charge to 4.6 V. An anomalous capacity was delivered by the oxygen redox, as observed from the O K-edge spectrum of the Z3 electrode (Fig. 6c). The data indicate that there was a change in the pre-edge of oxygen as the shoulder peak at approximately 536 eV disappeared during charge and reappeared following the discharge process, which is reversible. The variation in oxygen can explain the initial capacity delivered by the oxygen redox (O^{2-}/O^{1-}). As observed in the XPS spectra, there was a change in the C1s and O1s regions unlike for the Z0 electrode. In the O1s spectrum, there are three peaks such as for the Z0 electrode at the OCV; however, peak separation resulted in a new peak at 530 eV for the charged electrode. This new peak is assigned to superoxygen (O_2^{1-}), which is produced by the oxidation of oxygen bonded with Mn and Zn elements in the structure. As a result, the relative intensity of the MO (M: Mn and Zn) binding was reduced (Fig. S7). Therefore, the contraction of the unit cell during desodiation is responsible for the formation of the M–O^{1-} bond from the M–O^{2-} bond (Figure 4Sb). Because the ionic radius of O^{2-} is larger than that of O^{1-} (O: 1.52 Å, O^{2-}: 1.4 Å, O^{1-}: smaller than that of O^{2-}) because of the smaller number of electrons, it is possible to understand such variation in the lattice parameters. The above results reveal that the delivered first charge capacity is generated by oxidation of oxygen from O^{2-} to O^{1-}. The reversible reaction, reduction of oxygen from O^{1-} to O^{2-}, is evidenced in the XPS spectrum during discharge, as the new peak at 530 eV disappeared but MO (M: Mn and Zn) binding became strong again at 529 eV. A similar tendency was previously observed in the $Li_2Ru_{0.5}Sn_{0.5}O_3$ system, called oxygen redox activated by the $O^{2-/1-}$ pair [40]. Not only the reduction of oxygen from O^{1-} to O^{2-} but also $Mn^{4+/3+}$ contributes to the discharge capacity because the shift of the Mn K-edge is evident in the photon energy during discharge, even though the oxidation state of Mn remains higher than $Mn^{3.5+}$, which agrees with our discussion in Fig. 5b. We also compared the EXAFS for the Mn to see the local change in the structure resulted from the oxygen redox (Fig. 6d). Compared to the fresh electrode, the slight variation in the EXAFS spectrum after the charge is due to the local structural change caused by the oxidation of oxygen in the MO_6 environment.

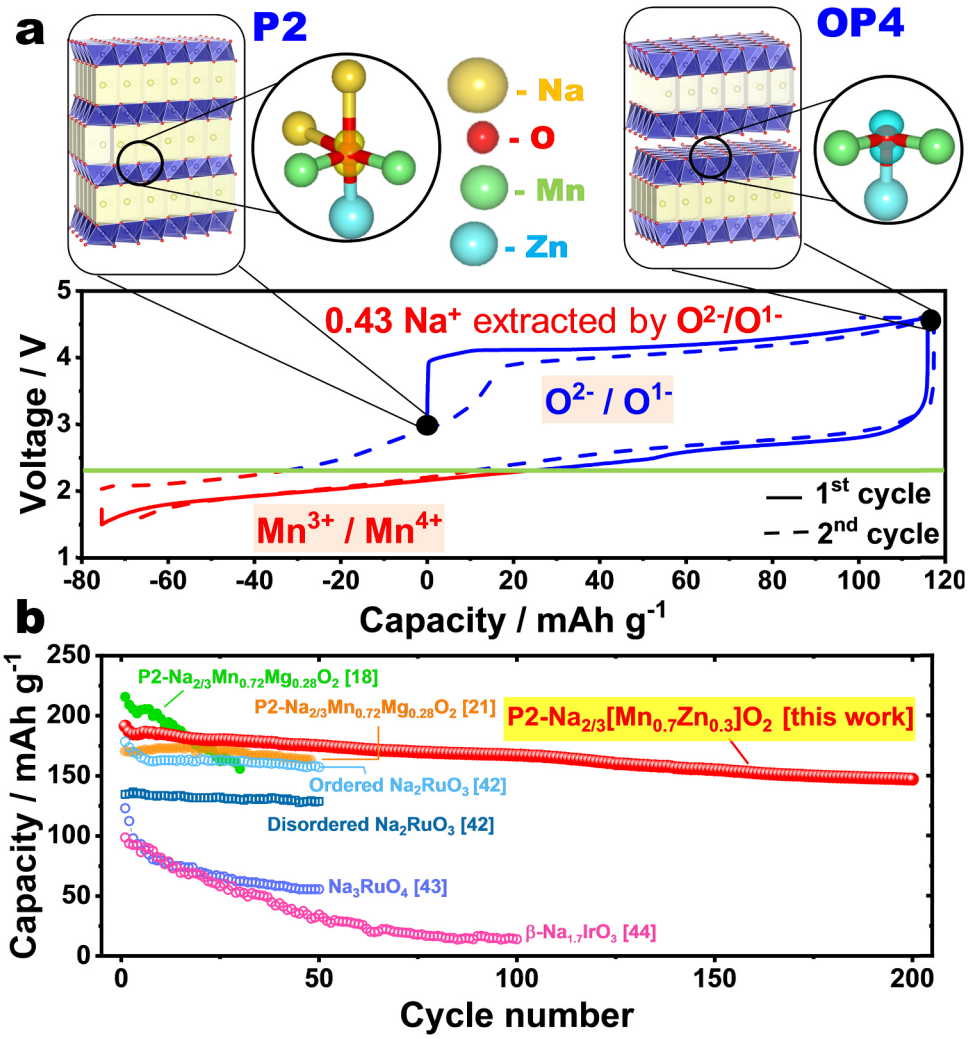

Fig. 7. (a) Scheme of the reaction mechanism of P2-$Na_{2/3}[Mn_{0.7}Zn_{0.3}]O_2$ electrodes, (b) comparison of cycle performance with reported oxygen-redox cathode materials for SIBs.

In our earlier work on Li-rich $Li[Li_{0.2}Ni_{0.13}Co_{0.13}Mn_{0.54}]O_2$ (or $0.5Li_2MnO_3$–$0.5Li[Co_{1/3}Ni_{1/3}Mn_{1/3}]O_2$), which releases oxygen at the first charge above 4.4 V versus Li^+/Li, we observed sediment of Li_2CO_3 on the surface of the active materials when discharged to 3 V [38]. For the $Na_{2/3}[Mn_{0.7}Zn_{0.3}]O_2$ activated by $O^{2-/1-}$ and $Mn^{3+/4+}$ redox pairs, fragments related to Na_2CO_3 as NaC_2^+ (m = 46.99) were not detected for the first charge and discharge (Fig. S8). However, Na_2O^+ (m = 61.98) was detected in the discharged electrode. This result supports the idea that the $Na_{2/3}[Mn_{0.7}Zn_{0.3}]O_2$ undergoes a reaction, not oxygen release, from the crystal structure that is activated by $O^{2-/1-}$ and $Mn^{3+/4+}$ redox pairs.

Fig. 7a further validates our finding concerning the reaction process for $Na_{2/3}[Mn_{0.7}Zn_{0.3}]O_2$. As we discussed in the introduction part, Zn has recently been used as a dopant to stabilize the structure of P2-type sodium cathode materials such as $Na_{0.66}Ni_{0.33-x}Zn_xMn_{0.67}O_2$ [22,23], $Na_{0.67}Mn_{0.6}Fe_{0.3}Zn_{0.1}O_2$ [25], and $Na_3Ni_{1.5}Zn_{0.5}SbO_6$ [24]. However, in all the reported works, the capacities were was generated by only transition metal redox, not by the oxygen redox which is inactive in those mentioned compounds. Different from those works, the introduction of Zn in $Na_{2/3}Mn_{1-x}Zn_xO_2$ compound resulted in oxygen redox followed by the transition metal redox. Although the first charge is mainly related to the $O^{2-/1-}$ redox pair, voltage plateaus are apparent. Specifically, the lower voltage plateau is attributed to the $Mn^{3+/4+}$ redox reaction and the upper one is attributed to the $O^{2-/1-}$ redox pair. Note that the capacity in the low-voltage region coincides with the oxidation of Mn from 3.5+ toward 4+. The reversible reaction is observed below 2.2 V, associated with the formation of the P′2 phase from the P2 phase. In contrast, the length of the upper voltage plateau gradually shortened with cycling. The oxygen redox reaction is likely to be interrupted by surface resistance of the electrode caused by the many types of sediment produced by oxidative decomposition of the electrolytic salt and solvents and dissolution of manganese during prolonged high-voltage operation. The above *operando* and *ex situ* XRD, XPS, XANES, and TOF-SIMS results are summarized in the reaction scheme for $Na_{2/3}[Mn_{0.7}Zn_{0.3}]O_2$ in Fig. 7a.

Because the average oxidation state of Mn is close to 4 + , electrochemical oxidation of oxygen in the compound generates a capacity above 4 V at the first charge, which gradually transforms the structure from P2 to OP4 though with low crystallinity. On discharge, the reduction of oxygen progresses to 2.2 V, and the OP4 phase is progressively recovered to the original P2 phase. Further reduction activates additional reduction of $Mn^{4+/3+}$, which results in another phase transition from the P2 to P′2 phase. Then, the phase transition P′2 ↔ P2 ↔ OP4 occurs reversibly throughout the cycles. As can be seen from Fig. 7b and Table S4 that compare recent oxygen-redox cathodes for sodium ion batteries, our material presented excellent cycling performance for 200 cycles. There are several works on oxygen redox reaction in $Na_{2/3}MnO_2$ compound doped with either Li [12] or Mg [18,21]. The differences of our work from those are that we use earth abundant Zn to activate the oxygen redox. Unlike $Na_{2/3}Mn_{1-x}Li_xO_2$ in which extraction of lithium is obvious during charge, Zn ions do not migrate from the transition metal layer during cycles for our $Na_{2/3}Mn_{0.7}Zn_{0.3}O_2$ compound, which was proven by *ex situ* XRD and ICP analysis (Fig. S5 and Table S2). More interestingly, compared to $Na_{2/3}Mn_{0.72}Mg_{0.28}O_2$ compound, the electronegativity of Zn (1.65 [41]) is higher than Mg (1.31 [41]), which, we believe, enhances the stabilization of the structure due to the covalent character of zinc with oxygen rather than magnesium with oxygen. As a result, our material displayed improved long-term performance for 200 cycles retaining 80% of its initial capacity that is the highest capacity retention among other oxygen redox-based cathodes for SIBs. In addition, compared with ruthenium [42,43] and iridium [44] based compounds our cathode is more earth-abundant.

The long-term structural stability was investigated using *ex situ* XRD of the extensively cycled Z0 and Z3 electrodes (Fig. S9). For the Z0 electrode, a new peak appeared at 34° 2θ, which can be assigned as Mn_3O_4. From the disassembled cells, it was confirmed that the separator turned a yellowish color because of the dissolved manganese in the electrolyte. The dissolution of Mn occurred because of HF attack of the active materials, especially at high voltage, such that Mn^{3+} was disproportionated into Mn^{2+} and Mn^{4+}, $2Mn^{3+} \rightarrow Mn^{2+}$ and Mn^{4+}, which is typically observed in spinel $LiMn_2O_4$ [45]. However, for the Z3 electrode, no additional peaks were observed in the XRD data and the separator remained colorless. Moreover, the HF attack was presumably prevented by the high oxidation state of Mn. Structural disproportion caused by the Jahn–Teller active Mn^{3+} ion was also suppressed by the electrochemically inactive Zn^{2+} ion in the structure.

4. Conclusion

In summary, we investigate the effect of Zn doping on P2-$Na_{2/3}MnO_2$ in an effort to improve its electrochemical properties. Our study reveal that Zn^{2+} ions substitute for Mn^{3+} ions, as they have similar ionic radius, and suppress the Jahn–Teller distortion. Moreover, the addition of Zn^{2+} ions increases the overall oxidation state of manganese. Notably, the initial charge profile of the Zn-doped electrodes differs from that of the Zn-free electrode, which is associated with oxygen redox. *Ex situ* XPS and XANES analyses reveal that the delivered capacity originates from a mixture of cathodic and anodic redox. *Operando* XRD analysis shows that the Zn-doped electrode undergoes a phase transformation of P′2 ↔ P2 ↔ OP4 during the initial cycle. *Ex situ* XRD analysis of the Z3 electrodes after different cycles shows that no structural arrangements occurs, unlike in the Li-rich system. In addition, ICP analysis of the pristine and charged electrodes confirms that Zn ions are not extracted from the structure. Our findings will thus guide researchers in considering oxygen redox to achieve increased capacity.

Acknowledgments

This research was supported by the International Research & Development Program of the National Research Foundation of Korea (NRF) funded by the Ministry of Science and ICT of Korea (NRF-2017K1A3A1A30084795, NRF-2015M3D1A1069713 and NRF-2017R1A2A2A05069634).

Appendix A. Supporting information

Supplementary data associated with this article can be found in the online version at doi:10.1016/j.nanoen.2019.02.042.

References

[1] B. Nykvist, M. Nilsson, Rapidly falling costs of battery packs for electric vehicles, Nat. Clim. Change 5 (2015) 329–332, https://doi.org/10.1038/nclimate2564.
[2] C. Vaalma, D. Buchholz, M. Weil, S. Passerini, A cost and resource analysis of sodium-ion batteries, Nat. Rev. Mater. 3 (2018) 18013, https://doi.org/10.1038/natrevmats.2018.13.
[3] N. Nitta, F. Wu, J.T. Lee, G. Yushin, Li-ion battery materials: present and future, Mater. Today 18 (2015) 252–264, https://doi.org/10.1016/j.mattod.2014.10.040.
[4] J. Rogelj, M. den Elzen, N. Höhne, T. Fransen, H. Fekete, H. Winkler, R. Schaeffer, F. Sha, K. Riahi, M. Meinshausen, Paris Agreement climate proposals need a boost to keep warming well below 2 °C, Nature 534 (2016) 631–639, https://doi.org/10.1038/nature18307.
[5] C. Delmas, Sodium and sodium-ion batteries: 50 years of research, Adv. Energy Mater. 8 (2018) 1703137, https://doi.org/10.1002/aenm.201703137.
[6] N. Yabuuchi, K. Kubota, M. Dahbi, S. Komaba, Research development on sodium-ion batteries, Chem. Rev. 114 (2014) 11636–11682, https://doi.org/10.1021/cr500192f.
[7] J.-Y. Hwang, S.-T. Myung, Y.-K. Sun, Sodium-ion batteries: present and future, Chem. Soc. Rev. 46 (2017) 3529–3614, https://doi.org/10.1039/C6CS00776G.
[8] C. Delmas, J. Braconnier, C. Fouassier, P. Hagenmuller, Electrochemical intercalation of sodium in Na_xCoO_2 bronzes, Solid State Ion. 3–4 (1981) 165–169, https://doi.org/10.1016/0167-2738(81)90076-X.
[9] Y. Mo, S.P. Ong, G. Ceder, Insights into diffusion mechanisms in P2 layered oxide materials by first-principles calculations, Chem. Mater. 26 (2014) 5208–5214, https://doi.org/10.1021/cm501563f.
[10] N. Ortiz-Vitoriano, N.E. Drewett, E. Gonzalo, T. Rojo, High performance

manganese-based layered oxide cathodes: overcoming the challenges of sodium ion batteries, Energy Environ. Sci. 10 (2017) 1051–1074, https://doi.org/10.1039/C7EE00566K.
[11] E. de la Llave, E. Talaie, E. Levi, P.K. Nayak, M. Dixit, P.T. Rao, P. Hartmann, F. Chesneau, D.T. Major, M. Greenstein, D. Aurbach, L.F. Nazar, Improving energy density and structural stability of manganese oxide cathodes for Na-ion batteries by structural lithium substitution, Chem. Mater. 28 (2016) 9064–9076, https://doi.org/10.1021/acs.chemmater.6b04078.
[12] N. Yabuuchi, R. Hara, M. Kajiyama, K. Kubota, T. Ishigaki, A. Hoshikawa, S. Komaba, New O2/P2-type Li-excess layered manganese oxides as promising multi-functional electrode materials for rechargeable Li/Na batteries, Adv. Energy Mater. 4 (2014) 1301453, https://doi.org/10.1002/aenm.201301453.
[13] N. Bucher, S. Hartung, J.B. Franklin, A.M. Wise, L.Y. Lim, H.-Y. Chen, J.N. Weker, M.F. Toney, M. Srinivasan, P2–$Na_xCo_yMn_{1-y}O_2$ ($y = 0, 0.1$) as cathode materials in sodium-ion batteries—effects of doping and morphology to enhance cycling stability, Chem. Mater. 28 (2016) 2041–2051, https://doi.org/10.1021/acs.chemmater.5b04557.
[14] W.-L. Pang, X.-H. Zhang, J.-Z. Guo, J.-Y. Li, X. Yan, B.-H. Hou, H.-Y. Guan, X.-L. Wu, P2-type $Na_{2/3}Mn_{1-x}Al_xO_2$ cathode material for sodium-ion batteries: Al-doped enhanced electrochemical properties and studies on the electrode kinetics, J. Power Sources 356 (2017) 80–88, https://doi.org/10.1016/j.jpowsour.2017.04.076.
[15] W. Kang, Z. Zhang, P.-K. Lee, T.-W. Ng, W. Li, Y. Tang, W. Zhang, C.-S. Lee, D.Y. Wai Yu, Copper substituted P2-type $Na_{0.67}Cu_xMn_{1-x}O_2$: a stable high-power sodium-ion battery cathode, J. Mater. Chem. A. 3 (2015) 22846–22852, https://doi.org/10.1039/C5TA06371J.
[16] N. Yabuuchi, M. Kajiyama, J. Iwatate, H. Nishikawa, S. Hitomi, R. Okuyama, R. Usui, Y. Yamada, S. Komaba, P2-type $Na_x[Fe_{1/2}Mn_{1/2}]O_2$ made from earth-abundant elements for rechargeable Na batteries, Nat. Mater. 11 (2012) 512–517, https://doi.org/10.1038/nmat3309.
[17] R.J. Clément, J. Billaud, A. Robert Armstrong, G. Singh, T. Rojo, P.G. Bruce, C.P. Grey, Structurally stable Mg-doped P2-$Na_{2/3}Mn_{1-y}Mg_yO_2$ sodium-ion battery cathodes with high rate performance: insights from electrochemical, NMR and diffraction studies, Energy Environ. Sci. 9 (2016) 3240–3251, https://doi.org/10.1039/C6EE01750A.
[18] N. Yabuuchi, R. Hara, K. Kubota, J. Paulsen, S. Kumakura, S. Komaba, A new electrode material for rechargeable sodium batteries: P2-type $Na_{2/3}[Mg_{0.28}Mn_{0.72}]O_2$ with anomalously high reversible capacity, J. Mater. Chem. A. 2 (2014) 16851–16855, https://doi.org/10.1039/C4TA04351K.
[19] N. Sharma, N. Tapia-Ruiz, G. Singh, A.R. Armstrong, J.C. Pramudita, H.E.A. Brand, J. Billaud, P.G. Bruce, T. Rojo, Rate dependent performance related to crystal structure evolution of $Na_{0.67}Mn_{0.8}Mg_{0.2}O_2$ in a sodium-ion battery, Chem. Mater. 27 (2015) 6976–6986, https://doi.org/10.1021/acs.chemmater.5b02142.
[20] J. Billaud, G. Singh, A.R. Armstrong, E. Gonzalo, V. Roddatis, M. Armand, T. Rojo, P.G. Bruce, $Na_{0.67}Mn_{1-x}Mg_xO_2$ ($0 \le x \le 0.2$): a high capacity cathode for sodium-ion batteries, Energy Environ. Sci. 7 (2014) 1387–1391, https://doi.org/10.1039/C4EE00465E.
[21] U. Maitra, R.A. House, J.W. Somerville, N. Tapia-Ruiz, J.G. Lozano, N. Guerrini, R. Hao, K. Luo, L. Jin, M.A. Pérez-Osorio, F. Massel, D.M. Pickup, S. Ramos, X. Lu, D.E. McNally, A.V. Chadwick, F. Giustino, T. Schmitt, L.C. Duda, M.R. Roberts, P.G. Bruce, Oxygen redox chemistry without excess alkali-metal ions in $Na_{2/3}[Mg_{0.28}Mn_{0.72}]O_2$, Nat. Chem. 10 (2018) 288–295, https://doi.org/10.1038/nchem.2923.
[22] X. Wu, J. Guo, D. Wang, G. Zhong, M.J. McDonald, Y. Yang, P2-type $Na_{0.66}Ni_{0.33-x}Zn_xMn_{0.67}O_2$ as new high-voltage cathode materials for sodium-ion batteries, J. Power Sources 281 (2015) 18–26, https://doi.org/10.1016/j.jpowsour.2014.12.083.
[23] X. Wu, G.-L. Xu, G. Zhong, Z. Gong, M.J. McDonald, S. Zheng, R. Fu, Z. Chen, K. Amine, Y. Yang, Insights into the effects of zinc doping on structural phase transition of P2-type sodium nickel manganese oxide cathodes for high-energy sodium ion batteries, ACS Appl. Mater. Interfaces 8 (2016) 22227–22237, https://doi.org/10.1021/acsami.6b06701.
[24] F. Aguesse, J.-M. Lopez del Amo, L. Otaegui, E. Goikolea, T. Rojo, G. Singh, Structural and electrochemical analysis of Zn doped $Na_3Ni_2SbO_6$ cathode for Na-ion battery, J. Power Sources 336 (2016) 186–195, https://doi.org/10.1016/j.jpowsour.2016.10.067.
[25] H. Xu, J. Zong, X. Liu, P2-type $Na_{0.67}Mn_{0.6}Fe_{0.4-x-y}Zn_xNi_yO_2$ cathode material with high-capacity for sodium-ion battery, Ionics 24 (2018) 1939–1946, https://doi.org/10.1007/s11581-018-2442-5.
[26] S. Kumakura, Y. Tahara, S. Sato, K. Kubota, S. Komaba, P′2-$Na_{2/3}Mn_{0.9}Me_{0.1}O_2$ (Me = Mg, Ti, Co, Ni, Cu, and Zn): correlation between orthorhombic distortion and electrochemical property, Chem. Mater. 29 (2017) 8958–8962, https://doi.org/10.1021/acs.chemmater.7b02772.
[27] A. Konarov, J.U. Choi, Z. Bakenov, S.-T. Myung, Revisit of layered sodium manganese oxides: achievement of high energy by Ni incorporation, J. Mater. Chem. A. 6 (2018) 8558–8567, https://doi.org/10.1039/C8TA02067A.
[28] T. Roisnel, J. Rodríguez-Carvajal, Full-. Man. (2002) 139.
[29] B. Ravel, M. Newville, *ATHENA*, *ARTEMIS*, *HEPHAESTUS*: data analysis for X-ray absorption spectroscopy using *IFEFFIT*, J. Synchrotron Radiat. 12 (2005) 537–541, https://doi.org/10.1107/S0909049505012719.
[30] G. Kresse, D. Joubert, From ultrasoft pseudopotentials to the projector augmented-wave method, Phys. Rev. B. 59 (1999) 1758–1775, https://doi.org/10.1103/PhysRevB.59.1758.
[31] G. Kresse, J. Furthmüller, Efficiency of ab-initio total energy calculations for metals and semiconductors using a plane-wave basis set, Comput. Mater. Sci. 6 (1996) 15–50, https://doi.org/10.1016/0927-0256(96)00008-0.
[32] G. Kresse, J. Furthmüller, Efficient iterative schemes for *ab initio* total-energy calculations using a plane-wave basis set, Phys. Rev. B. 54 (1996) 11169–11186, https://doi.org/10.1103/PhysRevB.54.11169.
[33] P.E. Blöchl, Projector augmented-wave method, Phys. Rev. B. 50 (1994) 17953–17979, https://doi.org/10.1103/PhysRevB.50.17953.
[34] J.P. Perdew, K. Burke, M. Ernzerhof, Generalized gradient approximation made simple, Phys. Rev. Lett. 77 (1996) 3865–3868, https://doi.org/10.1103/PhysRevLett.77.3865.
[35] D.-H. Seo, J. Lee, A. Urban, R. Malik, S. Kang, G. Ceder, The structural and chemical origin of the oxygen redox activity in layered and cation-disordered Li-excess cathode materials, Nat. Chem. 8 (2016) 692–697, https://doi.org/10.1038/nchem.2524.
[36] A. Van der Ven, J.C. Thomas, Q. Xu, J. Bhattacharya, Linking the electronic structure of solids to their thermodynamic and kinetic properties, Math. Comput. Simul. 80 (2010) 1393–1410, https://doi.org/10.1016/j.matcom.2009.08.008.
[37] S. Kumakura, Y. Tahara, K. Kubota, K. Chihara, S. Komaba, Sodium and manganese stoichiometry of P2-Type $Na_{2/3}MnO_2$, Angew. Chem. Int. Ed. 55 (2016) 12760–12763, https://doi.org/10.1002/anie.201606415.
[38] N. Yabuuchi, K. Yoshii, S.-T. Myung, I. Nakai, S. Komaba, Detailed studies of a high-capacity electrode material for rechargeable batteries, Li_2MnO_3 –$LiCo_{1/3}Ni_{1/3}Mn_{1/3}O_2$, J. Am. Chem. Soc. 133 (2011) 4404–4419, https://doi.org/10.1021/ja108588y.
[39] A. Ito, Y. Sato, T. Sanada, M. Hatano, H. Horie, Y. Ohsawa, In situ X-ray absorption spectroscopic study of Li-rich layered cathode material $Li[Ni_{0.17}Li_{0.2}Co_{0.07}Mn_{0.56}]O_2$, J. Power Sources 196 (2011) 6828–6834, https://doi.org/10.1016/j.jpowsour.2010.09.105.
[40] M. Sathiya, G. Rousse, K. Ramesha, C.P. Laisa, H. Vezin, M.T. Sougrati, M.-L. Doublet, D. Foix, D. Gonbeau, W. Walker, A.S. Prakash, M. Ben Hassine, L. Dupont, J.-M. Tarascon, Reversible anionic redox chemistry in high-capacity layered-oxide electrodes, Nat. Mater. 12 (2013) 827–835, https://doi.org/10.1038/nmat3699.
[41] A.L. Allred, Electronegativity values from thermochemical data, J. Inorg. Nucl. Chem. 17 (1961) 215–221, https://doi.org/10.1016/0022-1902(61)80142-5.
[42] B. Mortemard de Boisse, G. Liu, J. Ma, S. Nishimura, S.-C. Chung, H. Kiuchi, Y. Harada, J. Kikkawa, Y. Kobayashi, M. Okubo, A. Yamada, Intermediate honeycomb ordering to trigger oxygen redox chemistry in layered battery electrode, Nat. Commun. 7 (2016) 11397, https://doi.org/10.1038/ncomms11397.
[43] Y. Qiao, S. Guo, K. Zhu, P. Liu, X. Li, K. Jiang, C.-J. Sun, M. Chen, H. Zhou, Reversible anionic redox activity in Na_3RuO_4 cathodes: a prototype Na-rich layered oxide, Energy Environ. Sci. 11 (2018) 299–305, https://doi.org/10.1039/C7EE03554C.
[44] P.E. Pearce, G. Rousse, O.M. Karakulina, J. Hadermann, G. Van Tendeloo, D. Foix, F. Fauth, A.M. Abakumov, J.-M. Tarascon, β-$Na_{1.7}IrO_3$: a tridimensional Na-ion insertion material with a redox active oxygen network, Chem. Mater. 30 (2018) 3285–3293, https://doi.org/10.1021/acs.chemmater.8b00320.
[45] J.C. Hunter, Preparation of a new crystal form of manganese dioxide: λ-mno_2, J. Solid State Chem. 39 (1981) 142–147, https://doi.org/10.1016/0022-4596(81)90323-6.

Aishuak Konarov received his master's degree from the University of Waterloo in 2014. He is currently a Ph.D. candidate in the Department of NanoEngineering at Sejong University, South Korea, under the supervision of Professor Seung-Taek Myung. His research focuses on synthesis and characterization of active materials for lithium-ion, sodium-ion, and zinc-ion batteries, as well as lithium-sulfur batteries.

Jae Hyeon Jo is presently a Ph.D. candidate in the Department of NanoEngineering at Sejong University, South Korea, under the supervision of Professor Seung-Taek Myung. His research focuses on materials development in the fields of energy conversion and storage, such as cathode and anode materials for sodium ion batteries and zinc ion batteries.

Ji Ung Choi is presently a Ph.D. candidate in the Department of NanoEngineering at Sejong University, South Korea, under the supervision of Professor Seung-Taek Myung. His research focuses on materials development in the fields of energy conversion and storage, such as cathode materials for sodium ion batteries.

Zhumabay Bakenov is a Professor of Chemical Engineering at Nazarbayev University, a Founder of Institute of Batteries, and Director of the Center for Energy and Advanced Materials Science of National Laboratory Astana, Kazakhstan. He received his Doctor of Engineering (Chemical Engineering) degree from Tokyo Institute of Technology, Japan and the Ph.D. degree from the Kazakh National Academy of Science, Kazakhstan. His research interests are advanced energy storage and conversion systems; synthesis of functional nanomaterials for energy, environmental and biological applications.

Hitoshi Yashiro is a Vice President for the Graduate School of Arts and Sciences and Center of Community Project at Iwate University, Japan. He earned his bachelor's (1982) and Ph. D. (1994) degrees from Tohoku University, Japan. He was an international fellow at SRI International in 1991–1992. His research covers a variety of corrosion problems from the lithium-ion battery to nuclear power plants.

Jongsoon Kim received Ph. D. (2014) at the Seoul National University (SNU) and is currently an assistant professor in the Department of Nanotechnology and Advanced Materials Engineering at Sejong University, South Korea. His research focuses on the development of new electrode materials for Li/Na ion batteries using neutron/X-ray scattering with first-principle calculation.

Seung-Taek Myung is a Professor of Department of Nanotechnology and Advanced Materials Engineering at Sejong University, South Korea. Before 2011, he affiliated at VK (principal engineer), 3 M (seinor engineer), and Iwate University (assistant professor). He received his Ph.D. degree in Chemical Engineering from Iwate University, Japan, in 2003. His research interests include the development of electro-active materials and corrosion of current collectors of rechargeable lithium and sodium ion batteries.